

LOW FREQUENCY RADIO–FIR CORRELATION IN NORMAL GALAXIES AT ~ 1 KPC SCALES

ARITRA BASU, SUBHASHIS ROY AND DIPANJAN MITRA

National Center for Radio Astrophysics, TIFR, Pune University Campus, Ganeshkhind Road, Pune - 411007
 aritra@ncra.tifr.res.in (AB); roy@ncra.tifr.res.in (SR); dmitra@ncra.tifr.res.in (DM)

Accepted to be published in ApJ, July 10, 2012

ABSTRACT

We study the radio–FIR correlation between the nonthermal (synchrotron) radio continuum emission at $\lambda 90$ cm (333 MHz) and the far infrared emission due to cool (~ 20 K) dust at $\lambda 70$ μ m in spatially resolved normal galaxies at scales of ~ 1 kpc. The slope of the radio–FIR correlation significantly differs between the arm and interarm regions. However, this change is not evident at a lower wavelength of $\lambda 20$ cm (1.4 GHz). We find the slope of the correlation in the arm to be 0.8 ± 0.12 and we use this to determine the coupling between equipartition magnetic field (B_{eq}) and gas density (ρ_{gas}) as $B_{\text{eq}} \propto \rho_{\text{gas}}^{0.51 \pm 0.12}$. This is close to what is predicted by MHD simulations of turbulent ISM, provided the same region produces both the radio and far infrared emission. We argue that at 1 kpc scales this condition is satisfied for radio emission at 1.4 GHz and may not be satisfied at 333 MHz. Change of slope observed in the interarm region could be caused by propagation of low energy (~ 1.5 GeV) and long lived ($\sim 10^8$ yr) cosmic ray electrons at 333 MHz.

Subject headings: techniques: image processing – cosmic rays – dust – galaxies : ISM – galaxies : spiral – infrared : galaxies – radio continuum : galaxies

1. INTRODUCTION

The radio–far infrared (FIR) correlation in normal galaxies was first observed by van der Kruit (1971, 1973) and later extended by the IRAS mission. Subsequently it was established that the correlation holds good (within a factor of 2) over five orders of magnitude in radio and FIR luminosity (Condon 1992; Yun et al. 2001) for a wide morphological class of galaxies like, spirals, irregulars and dwarfs (Wunderlich et al. 1987; Dressel 1988; Price & Duric 1992) on global scales. Based on spatially resolved studies of normal and irregular galaxies it is seen that the correlation holds even at scales of few tens to hundreds of parsecs (see e.g. Beck & Golla 1988; Xu et al. 1992; Hoernes et al. 1998; Murgia et al. 2005; Tabatabaei et al. 2007a; Hughes et al. 2006; Murphy et al. 2006a; Paladino et al. 2006; Paladino, Murgia & Orrù 2009; Dumas et al. 2011).

The basic model that connects these two regimes of emission is via star formation (Harwit & Pacini 1975). The radio continuum emission arises due to synchrotron emission (henceforth nonthermal emission) from relativistic electrons, produced in supernova remnants. A good fraction of them originate from massive ($\gtrsim 10 M_{\odot}$), short lived ($\lesssim 10^6$ yr) stars. The FIR emission arises from re-radiation by dust heated due to ultra violet (UV) photons emitted by the above population of stars. Though the cause of the correlation is well understood, the tightness over several orders of magnitude still remains puzzling. Many models explaining the correlation require close coupling between the magnetic field (B) and the gas density (ρ_{gas}) of the form, $B \propto \rho_{\text{gas}}^{\kappa}$ (see e.g., Helou & Bicay 1993; Niklas & Beck 1997; Thompson et al. 2006). Such a coupling can be established by magnetohydrodynamic (MHD) turbulence of the interstellar medium (ISM) (see Chandrasekhar & Fermi 1953; Cho & Vishniac 2000;

Cho, Lazarian & Vishniac 2003; Groves et al. 2003). Numerical simulations by Cho & Vishniac (2000) revealed that $\kappa = 0.5$ is a manifestation of the equipartition condition, i.e, in steady MHD turbulence the magnetic field energy density and the energy density of the gas are similar. Similar values of κ have been found through observations of magnetic field by Zeeman splitting observations in molecular clouds by Crutcher (1999), also by using equipartition magnetic field and molecular gas observations in external galaxies by Niklas & Beck (1997) and in Milky Way and M31 by Berkhuijsen (1997). Alternatively, the slope of the radio–FIR correlation has been used to find κ , where $\kappa \sim 0.4$ – 0.6 (Niklas & Beck 1997; Hoernes et al. 1998; Dumas et al. 2011).

So far, spatially resolved and global study of the correlation has been done primarily using radio emission at 1.4 GHz and higher frequencies. The only low frequency study done at 150 MHz (Cox et al. 1988), confirms that on global scales the radio–FIR correlation holds good and is similar to what is seen at 1.4 GHz. To our knowledge, no low frequency (< 1.4 GHz, such as 333 MHz) spatially resolved study of the radio–FIR correlation exists in the literature. The motivation to do such a study arises from the fact that at lower frequencies the emission is largely nonthermal, hence better exhibiting the relation between magnetic field and star formation. Secondly, since the cosmic ray electrons (CRE) propagate larger distances in the galaxies at lower frequencies, it is important to assess how that affects the form of the radio–FIR correlation.

In this paper, we present spatially resolved study of the radio–FIR correlation for four normal galaxies, NGC 4736, NGC 5055, NGC 5236 and NGC 6946 at spatial resolution of ~ 1 – 1.5 kpc with radio observations made at 333 MHz ($\lambda 90$ cm) and 1.4 GHz ($\lambda 20$ cm). We also estimate the value of κ and verify the equipartition assumptions. In Section 2 we discuss the various sources of maps used in this work and also define the parameter ‘ q ’

TABLE 1
THE SAMPLE GALAXIES.

Name	Morphological type	Angular size (D ₂₅)(')	<i>i</i> (°)	Distance (Mpc)	FIR $\lambda 70 \mu\text{m}$	$\lambda 90 \text{cm}$	Radio $\lambda 20 \text{cm}$
(1)	(2)	(3)	(4)	(5)	(6)	(7)	(8)
NGC 4736	SAab	11.2×9.1	41	4.66 ¹	SINGS	GMRT	Westerbork ^a SINGS (1374.5 MHz) ⁴
NGC 5055	SAbc	12.6×7.2	59	9.2 [†]	SINGS	GMRT	Westerbork SINGS (1696 MHz) ⁴
NGC 5236	SABc	11.2×11	24	4.51 ²	SINGS	GMRT	VLA ^b CD array (1452 MHz) ⁵
NGC 6946	SABcd	11.5×9.8	33	6.8 ³	SINGS	GMRT	VLA C+D array (1465 MHz) ⁶

In column (3) D₂₅ refers to the optical diameter measured at the 25 magnitude arcsec⁻² contour from de Vaucouleurs et al. (1991). Column (4) gives the inclination angle (*i*) defined such that 0° is face-on. Distances in column (5) are taken from: ¹ Karachentsev et al. (2003), ² Karachentsev et al. (2002), ³ Karachentsev, Sharina & Huchtmeier (2000) and the NED [†]. Column (6) and (7) are the sources of data for the FIR maps and 333 MHz ($\lambda 90 \text{cm}$) maps respectively. Column 8 are the data available at a higher frequency near 1 GHz ($\lambda 20 \text{cm}$): ⁴ Braun et al. (2007), ⁵ VLA archival data using the CD array configuration (project code : AS325), ⁶ VLA archival map by combining interferometric data from C and D array, Beck (2007).

^aThe Westerbork Synthesis Radio Telescope (WSRT) is operated by the Netherlands Foundation for Research in Astronomy (NFRA) with financial support from the Netherlands Organization for scientific research (NWO).

^bThe Very Large Array (VLA) is operated by the NRAO. The NRAO is a facility of the National Science Foundation operated under cooperative agreement by Associated Universities, Inc.

which is used to quantify the correlation. In Section 3 we present our results on spatially resolved radio–FIR correlation using far infrared emission at $\lambda 70 \mu\text{m}$ and radio emission at $\lambda 20 \text{cm}$ and $\lambda 90 \text{cm}$. We discuss our results in Section 4.

2. DATA ANALYSIS

The four galaxies in the sample for this study was chosen from Basu et al. (2012). The large angular size of the galaxies ensure enough independent regions to carry out spatially resolved study. Our sample comprises of the galaxies NGC 4736, NGC 5055, NGC 5236 and NGC 6946. Table 1 summarizes the salient features of our sample and the various sources of obtaining the archival data.

To study the radio–FIR correlation using nonthermal radio emission, a thorough separation of thermal radio emission is needed. We used nonthermal radio continuum maps at $\lambda 90 \text{cm}$ and $\lambda 20 \text{cm}$ after separating the thermal free–free component mainly originating from HII regions in recent star formation sites. Details of observation and data analysis are discussed in Basu et al. (2012). The thermal emission was estimated using the technique developed by Tabatabaei et al. (2007b), wherein, the dust extinction-corrected H α map is used as a template for the thermal free-free emission. This is then extrapolated to the desired radio frequency and subtracted from the total emission map. The $\lambda 90 \text{cm}$ maps were obtained using the Giant Meterwave Radio Telescope (GMRT) while the $\lambda 20 \text{cm}$ maps were obtained using archival data from various assorted sources (see Table 1). The nonthermal maps had 40 arcsec resolution with 9 arcsec pixel size. We scaled the flux of each galaxy to a common frequency of 1.4 GHz using the spectral index map obtained from the 333 MHz and near 1 GHz images for each pixel.

The galaxies were observed in the far-infrared by the *Spitzer* at $\lambda 70 \mu\text{m}$ as a part of the *Spitzer* Infrared Nearby Galaxy Survey (SINGS; Kennicutt et al. 2003) using the Multiband Imaging Photometer for *Spitzer* (MIPS; Rieke et al. 2004). The images were obtained from the publicly available database in SINGS Data Re-

lease 5¹. The $\lambda 70 \mu\text{m}$ images have a pixel size of 4.5 arcsec and a point spread function (PSF) of about 16 arcsec. These were convolved to the resolution of nonthermal radio maps (40 arcsec) and re-gridded to a common pixel size of 9 arcsec. All the maps were then aligned to the same coordinate system.

For the present study, the flux density per beam for the radio and FIR maps were determined within an area of ~ 40 arcsec diameter, with the adjacent region being about one beam away to ensure independence. Pixels with brightness above 2σ (σ is the *rms* noise in the map) were considered for the analysis. We estimate the slope of the radio–FIR and the quantity ‘*q*’ introduced by Helou, Soifer & Rowan-Robinson (1985).

The parameter *q* is used as a measure of the radio–FIR correlation, where its dispersion indicates the tightness of the correlation. Conventionally it is defined as the logarithm of the ratio of total FIR flux between $\lambda 40 \mu\text{m}$ and $\lambda 120 \mu\text{m}$ and the radio flux measured at 1.4 GHz. However, we define *q* as per Appleton et al. (2004) using FIR flux density at $\lambda 70 \mu\text{m}$, such that,

$$q_\lambda = \log_{10} (S_{70\mu\text{m}}/S_\lambda)$$

where, λ is the radio wavelength (here, $\lambda = 20 \text{cm}$ or 90cm) and $S_{70\mu\text{m}}$ and S_λ are the flux densities of $\lambda 70 \mu\text{m}$ and radio wavelength respectively. The FIR emission from galaxies between $\lambda 40 \mu\text{m}$ and $\lambda 120 \mu\text{m}$ is dominated by the emission from cool dust with dust temperature, $T_{\text{dust}} \sim 20 \text{K}$ (see e.g. Xu et al. 1992; Hoernes et al. 1998; Tabatabaei et al. 2007b; Basu et al. 2012). The peak of this emission occurs at about $\lambda 100 \mu\text{m}$. Note that a black body at $\sim 20 \text{K}$ peaks at about $\lambda 145 \mu\text{m}$, but a grey body ($\lambda^{-\beta} B_\lambda(T)$, where $\beta = 2$ is the dust emissivity index and $B_\lambda(T)$ is the Planck function) has a peak at $\sim \lambda 100 \mu\text{m}$. The maps at $\lambda 70 \mu\text{m}$, which are nearest available to $\lambda 100 \mu\text{m}$, essentially traces this component of the dust. Using monochromatic $\lambda 70 \mu\text{m}$ emission to study the radio–FIR correlation does not affect the conclusions significantly, except for a slight increase in the dispersion (Murphy et al. 2006a).

¹ <http://data.spitzer.caltech.edu/popular/sings/>

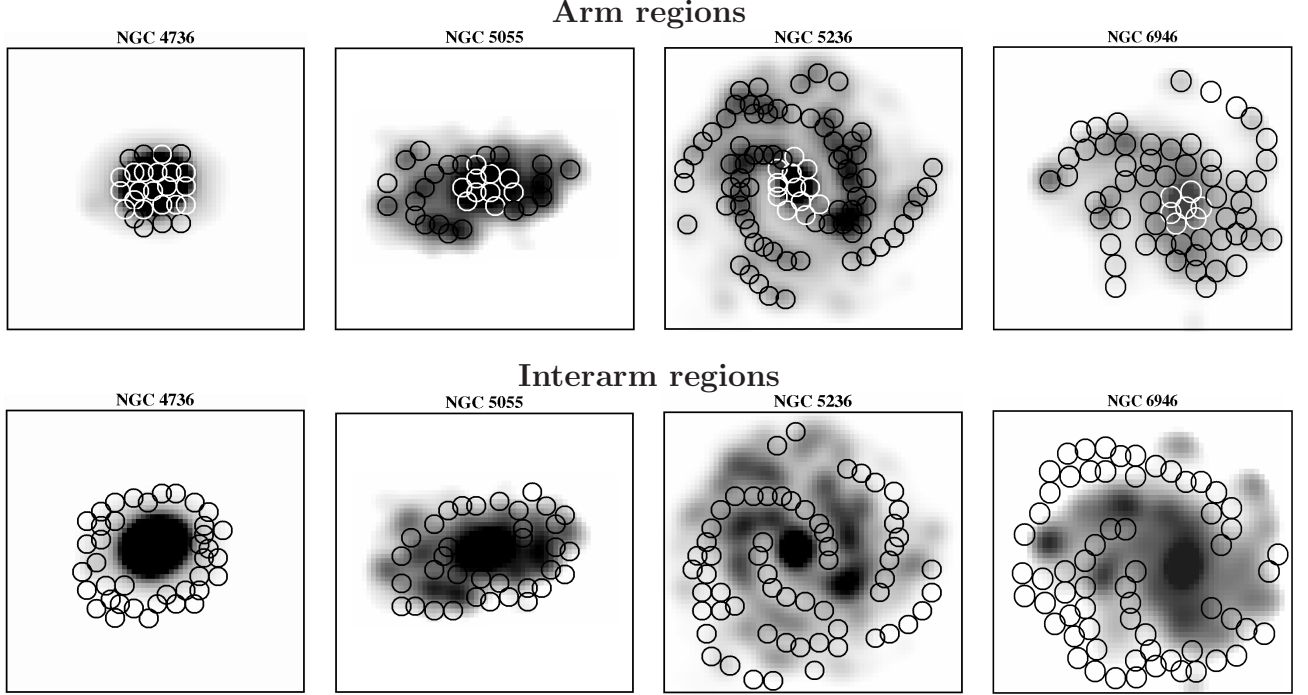


FIG. 1.— Overlay of ~ 40 arcsec beams (marked in circles) on the $H\alpha$ images^a smoothed to 40 arcsec. The top and lower panels shows the arm and the interarm regions respectively (see Section 3 for details).

^aThe images were downloaded from the NED for the galaxies NGC 4736 (1-m Jacobus Kapteyn Telescope (JKT) at La Palma with filter Ha6570; Knapen et al. 2004), NGC 5055 (2.3-m telescope at KPNO, filter: 6580) and NGC 5236 (0.9-m telescope at CTIO, filter: 6563). For NGC 6946 the image was downloaded from the SINGS website.

TABLE 2

INTEGRATED FLUX DENSITIES OF THE GALAXIES AT $\lambda 90$ CM (333 MHz; BASU ET AL. 2012), $\lambda 20$ CM (1400 MHz; SPECTRAL INDEX SCALED FROM DATA GIVEN IN COLUMN 8 OF TABLE 1) AND $\lambda 70$ μ M (TAKEN FROM THE NED). THE MAP NOISE (σ) FOR THE 40 ARCSEC RESOLUTION IMAGES ARE ALSO GIVEN.

Name	$S_{90\text{cm}}$ Jy	$\sigma_{90\text{cm}}$ mJy beam ⁻¹	$S_{20\text{cm}}$ Jy	$\sigma_{20\text{cm}}$ mJy beam ⁻¹	$S_{70\mu\text{m}}$ Jy	$\sigma_{70\mu\text{m}}$ mJy beam ⁻¹
NGC 4736	0.9 ± 0.06	2	0.31 ± 0.03	0.35	93.93 ± 7.34	15
NGC 5055	2.3 ± 0.13	3	0.41 ± 0.05	0.4	72.57 ± 5.16	15
NGC 5236	6.86 ± 0.62	2.5	2.36 ± 0.18	0.3	312.0 ± 15.6	30
NGC 6946	4.3 ± 0.24	1	1.5 ± 0.1	0.2	207.2 ± 16.1	25

TABLE 3

SUMMARY OF THE VALUES OF q_λ AND THE FITTED PARAMETERS FOR EACH OF THE GALAXIES. COLUMNS 3, 4 AND 5, 6 ARE THE MEAN VALUES OF q_λ AND THEIR DISPERSION AT $\lambda 20\text{cm}$ AND $\lambda 90\text{cm}$ RESPECTIVELY AS SHOWN IN FIGURE 2. THE VALUE OF q_λ WAS COMPUTED USING THE FLUX DENSITY WITHIN ONE BEAM OF FWHM ~ 40 ARCSEC. COLUMNS 7 AND 9 ARE THE FITTED VALUES FOR q_λ , WHILE COLUMNS 8 AND 10 ARE THE SLOPES OF THE RADIO–FIR CORRELATION. HERE, $a_{20\text{cm}}$, $b_{20\text{cm}}$ AND $a_{90\text{cm}}$, $b_{90\text{cm}}$ ARE THE PARAMETERS a AND b IN THE FITTED EQUATION, $S_{\text{radio}} = aS_{\text{IR}}^b$, AT WAVELENGTHS 20 CM AND 90 CM RESPECTIVELY.

Name		$\langle q_{20\text{cm}} \rangle$	$\sigma_{q_{20\text{cm}}}$	$\langle q_{90\text{cm}} \rangle$	$\sigma_{q_{90\text{cm}}}$	$S_{\text{radio}} = aS_{\text{IR}}^b$			
(1)	(2)	(3)	(4)	(5)	(6)	$-\log(a_{20\text{cm}})$	$b_{20\text{cm}}$	$-\log(a_{90\text{cm}})$	$b_{90\text{cm}}$
NGC 4736	arm:	2.45	0.12	2.01	0.20	2.28±0.02	0.73±0.04	1.71±0.03	0.49±0.04
	interarm:	2.46	0.15	1.46	0.23	2.41±0.04	1.13±0.12	1.71±0.03	0.28±0.04
NGC 5055	arm:	2.26	0.14	1.59	0.20	2.14±0.02	0.64±0.03	1.44±0.02	0.44±0.03
	interarm:	2.03	0.16	1.27	0.24	2.10±0.01	0.53±0.03	1.38±0.01	0.30±0.04
NGC 5236	arm:	2.32	0.14	1.92	0.20	2.27±0.04	0.92±0.04	1.71±0.03	0.66±0.04
	interarm:	2.13	0.20	1.60	0.26	2.08±0.03	0.76±0.05	1.50±0.02	0.40±0.04
NGC 6946	arm:	2.31	0.10	1.81	0.14	2.26±0.02	0.87±0.04	1.69±0.02	0.71±0.04
	interarm:	1.97	0.19	1.32	0.32	2.07±0.01	0.64±0.03	1.52±0.01	0.34±0.02

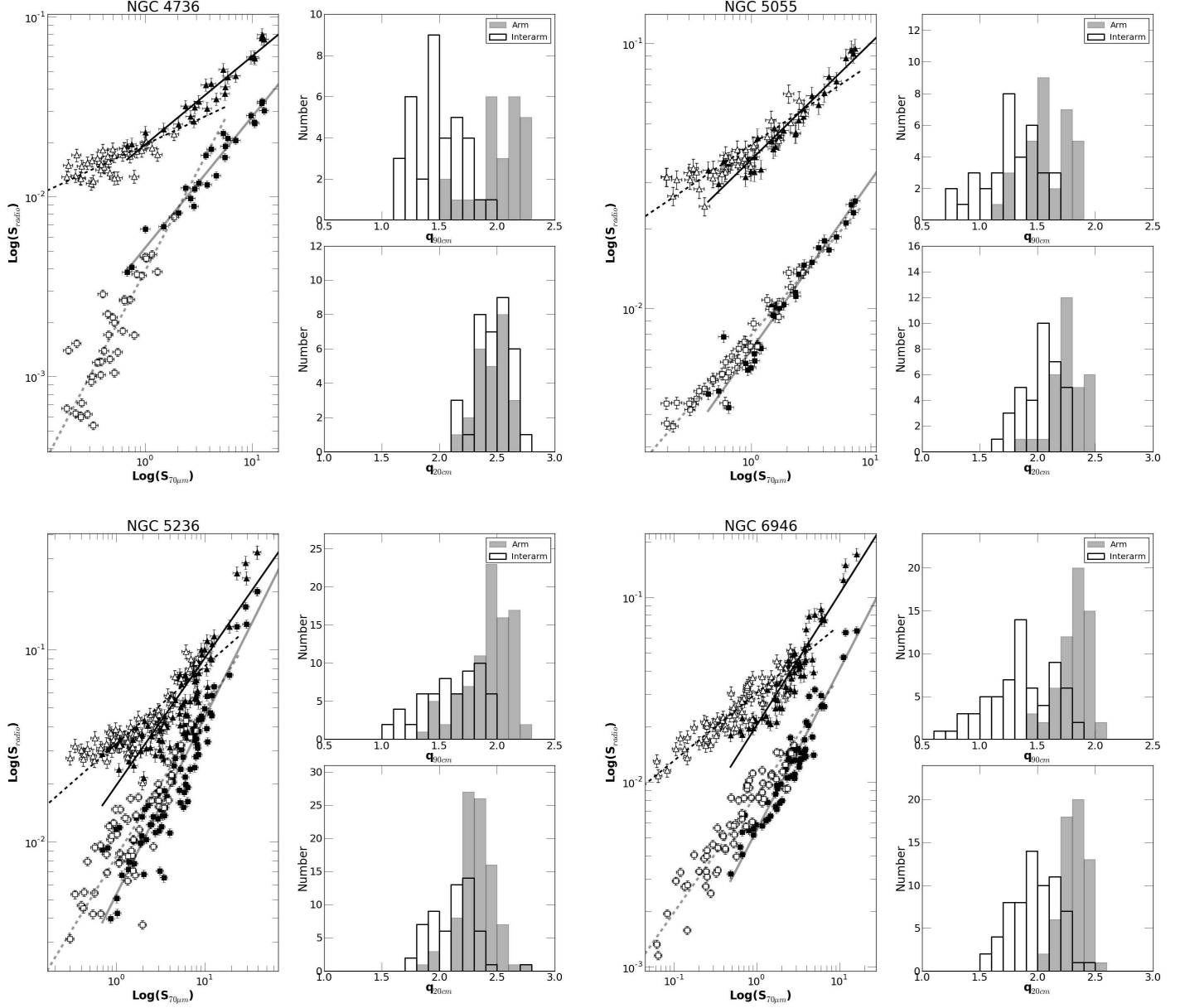


FIG. 2.— The figure shows the radio intensity vs. $\lambda 70 \mu\text{m}$ FIR intensity (in Jy beam^{-1}). The triangles are for $\lambda 90$ cm and squares are for $\lambda 20$ cm. The filled symbols are for arms and unfilled symbols are for interarms. The histograms are the distribution of $q_{90\text{cm}}$ and $q_{20\text{cm}}$, where arms are shown with filled grey and interarms with unfilled histograms. The lines are the fit to the data of the form $S_{\text{radio}} = a \times S_{70\mu\text{m}}^b$ (See Table 3). The solid and dashed lines are fit to the arm and interarm regions. Black lines are for $\lambda 90$ cm, while grey lines are for $\lambda 20$ cm.

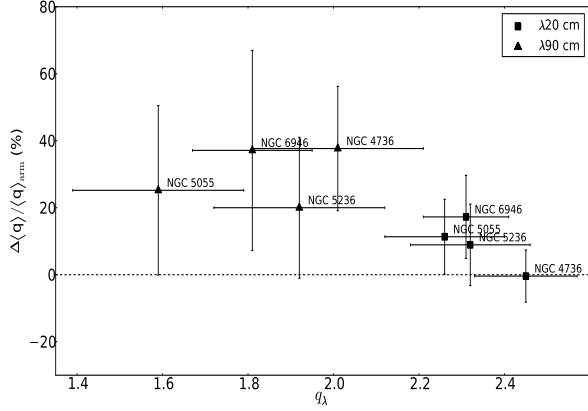


FIG. 3.— The percentage change in the value of $\langle q_\lambda \rangle$ between arms and interarms. Here, $\Delta\langle q \rangle = \langle q_\lambda \rangle_{\text{arm}} - \langle q_\lambda \rangle_{\text{interarm}}$ for each of the sample galaxies. The triangles are for $\lambda 90\text{ cm}$ and squares are for $\lambda 20\text{ cm}$. The mean change in the value of $q_{20\text{ cm}}$ between arms and interarms is ~ 10 percent, while $q_{90\text{ cm}}$ changes by ~ 30 percent.

3. RESULTS

The spatially resolved study of the radio-FIR correlation was done by broadly classifying the emission from arm (including the central region) and interarm regions of these galaxies. The arms were identified from the $\text{H}\alpha$ images for each galaxy. For the ringed galaxy NGC 4736, which has no prominent arms, the star forming ring was taken as the arm. The arm and the interarm regions used in our analysis are plotted as circles which are overlaid on the 40 arcsec $\text{H}\alpha$ images in Figure 1. The quantity q_λ was computed within each such region. Note that the calibration uncertainty at $\lambda 70\text{ }\mu\text{m}$ could be ~ 20 per cent (Murphy et al. 2006a). This would lead to a systematic error of about 10 per cent in the values of q_λ .

Table 2 gives the total flux density (in Jy) and map rms noise of the 40 arcsec images (in mJy beam^{-1}) of the galaxies. The galaxy integrated mean values of $q_{20\text{ cm}}$ are 2.48 ± 0.1 , 2.25 ± 0.07 , 2.12 ± 0.06 and 2.14 ± 0.07 , for the galaxies NGC 4736, NGC 5055, NGC 5236 and NGC 6946 respectively. The $q_{90\text{ cm}}$ are 2.02 ± 0.07 , 1.5 ± 0.1 , 1.66 ± 0.09 and 1.68 ± 0.08 respectively. However, the spatially resolved estimates of $q_{20\text{ cm}}$ and $q_{90\text{ cm}}$ suggests that their values vary between arm and interarm regions. Figure 2 shows the brightness of the nonthermal radio emission with the far infrared emission at $\lambda 70\text{ }\mu\text{m}$, both in units of Jy beam^{-1} , for all the four galaxies. The figure also shows the distribution of q_λ for $\lambda 20\text{ cm}$ and $\lambda 90\text{ cm}$. It was seen that the star forming, gas rich spiral arms of the galaxies showed higher values for q_λ when compared to the adjacent low star forming interarm regions. Table 3 summarizes the mean value of the quantity q_λ and its dispersion for arm and interarm regions.

The mean value in the arms for all the galaxies were found to be, $\langle q_{20\text{ cm}} \rangle_{\text{arm}} = 2.32$ with a narrow dispersion of $\sigma_{q_{20\text{ cm}, \text{arm}}} = 0.14$, while for the interarms $\langle q_{20\text{ cm}} \rangle_{\text{interarm}} = 2.15$ and $\sigma_{q_{20\text{ cm}, \text{interarm}}} = 0.3$. At $\lambda 90\text{ cm}$, we find the $\langle q_{90\text{ cm}} \rangle_{\text{arm}} = 1.85$ with $\sigma_{q_{90\text{ cm}, \text{arm}}} = 0.22$ and $\langle q_{90\text{ cm}} \rangle_{\text{interarm}} = 1.43$ and $\sigma_{q_{90\text{ cm}, \text{interarm}}} = 0.3$. Figure 3 shows the percentage change in the value of q_λ between arms and interarms for each of the galaxies, where $\Delta q = \langle q_\lambda \rangle_{\text{arm}} - \langle q_\lambda \rangle_{\text{interarm}}$. The squares are for

$\lambda 20\text{ cm}$ and triangles are for $\lambda 90\text{ cm}$. The mean of the $q_{20\text{ cm}}$ changes slightly, by about 9 percent, between arms and interarms, however, this change is significant with > 99.9 percent confidence using Kolmogorov-Smirnov test. At $\lambda 90\text{ cm}$, the change in the value of $\langle q_\lambda \rangle$ between arm and interarm regions are much pronounced with $\Delta q \sim 30$ percent.

3.1. Fit to the radio and IR flux densities

The data were fitted using the form $S_{\text{radio}} = a \times S_{\text{IR}}^b$, where, S_{radio} is the flux density of the radio emission at $\lambda 20\text{ cm}$ and $\lambda 90\text{ cm}$, and S_{IR} is the flux density of the $\lambda 70\text{ }\mu\text{m}$ infrared emission. The fitting parameter ‘ a ’ is an estimate for q_λ , where $q_\lambda = -\log_{10} a$, such that $\log_{10} S_\lambda = -q_\lambda + b \times \log_{10} S_{\text{IR}}$. The slope of the radio-infrared correlation is given by the parameter ‘ b ’. Separate fits were done for arm and interarm regions using ordinary least-square ‘bisector method’ (Isobe et al. 1990) in the log-log plane. The parameters obtained are summarized in Table 2 in the last four columns for $\lambda 20\text{ cm}$ and $\lambda 90\text{ cm}$. The values of $q_{20\text{ cm}}$ and $q_{90\text{ cm}}$ are in good agreement with the mean values obtained from the respective distribution. The fitted parameters are plotted in Figure 2. The black lines are for fits at $\lambda 90\text{ cm}$ and the grey lines are at $\lambda 20\text{ cm}$. The solid lines are fit to the arm regions only and the dashed lines are for the interarms. All the correlations are highly significant in our case with Pearson’s correlation coefficient, $r > 0.8$ (and $r > 0.9$ in most of the cases), except for interarm regions of NGC 4736 at $\lambda 90\text{ cm}$, where $r = 0.68$.

The slope of the $\lambda 20\text{ cm}$ and $\lambda 70\text{ }\mu\text{m}$ flux density for the arm regions for all the galaxies lies between $\sim 0.65 - 0.9$. However, for the interarm regions the slope is slightly shallower, lying in the range $0.55 - 1$. The mean value of the parameters for arm and interarm after the fit can be written as,

$$\log_{10} S_{20\text{ cm}} = -(2.24 \pm 0.05) + (0.8 \pm 0.08) \log_{10} S_{70\text{ }\mu\text{m}} \quad \text{for arm} \quad (1)$$

$$\log_{10} S_{20\text{ cm}} = -(2.17 \pm 0.05) + (0.76 \pm 0.14) \log_{10} S_{70\text{ }\mu\text{m}} \quad \text{for interarm} \quad (2)$$

The fitted value of $q_{20\text{ cm}}$ and the slope differs slightly from arms to interarms.

At $\lambda 90\text{ cm}$, we find that the slope lies in the range $\sim 0.45 - 0.7$ for the arms, whereas in the interarm region the slope lies in the range $\sim 0.3 - 0.4$. The slopes are much flatter than at $\lambda 20\text{ cm}$. The mean values of the fitted parameters are found to be,

$$\log_{10} S_{90\text{ cm}} = -(1.64 \pm 0.05) + (0.6 \pm 0.1) \log_{10} S_{70\text{ }\mu\text{m}} \quad \text{for arm} \quad (3)$$

$$\log_{10} S_{90\text{ cm}} = -(1.53 \pm 0.04) + (0.33 \pm 0.07) \log_{10} S_{70\text{ }\mu\text{m}} \quad \text{for interarm} \quad (4)$$

There is a significant change in the value of $q_{90\text{ cm}}$ and the slope between the arm and the interarm regions.

3.2. q vs. α_{nt}

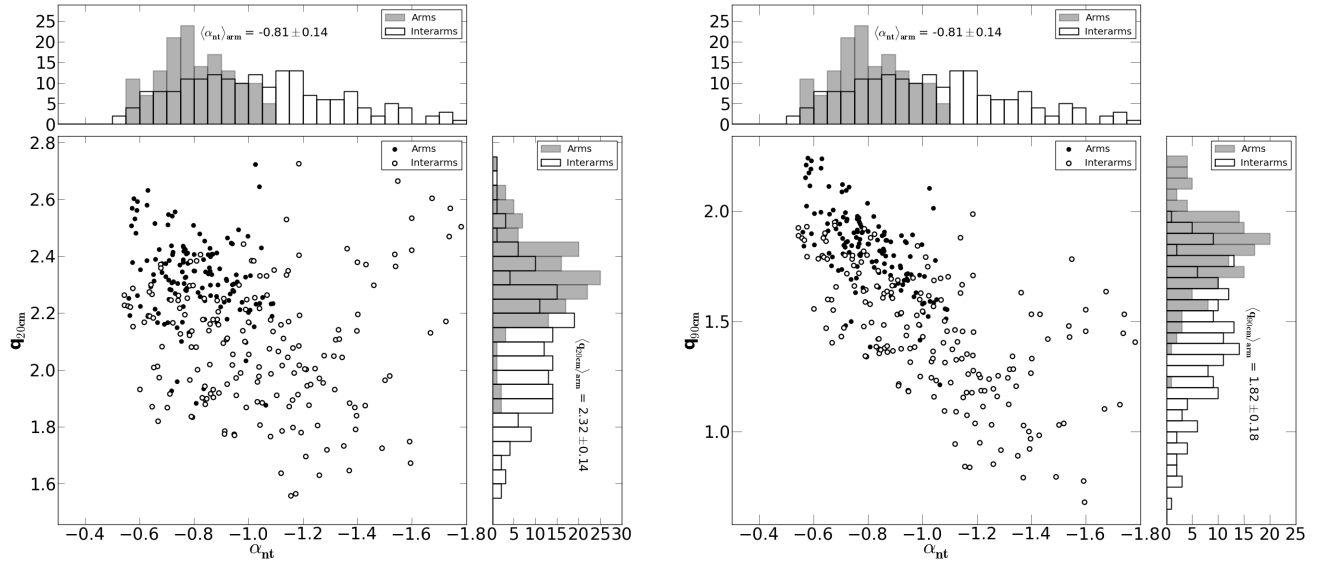


FIG. 4.— The figure shows the distribution of α_{nt} with $q_{20\text{cm}}$ (left) and $q_{90\text{cm}}$ (right). The top panel shows the distribution of α_{nt} estimated from $\lambda 90\text{cm}$ and $\lambda 20\text{cm}$ nonthermal emission radio maps within an area of $40 \times 40 \text{ arcsec}^2$ and a step size of 0.05, while the right side horizontal panel shows the distribution of q_λ within the same area and bin size of 0.05. The filled circles and histograms are for the arms and unfilled circles and histograms are for interarm regions for all the 4 galaxies combined.

The quantity ‘ q_λ ’ can be expressed in terms of CRe escape timescale (τ_{esc}) and synchrotron timescale (τ_{syn}) as $q_\lambda \propto \log(\tau_{\text{syn}}/\tau_{\text{esc}})$ (Murgia et al. 2005; Paladino et al. 2006). CRe emitting for these timescales also determines the variations in nonthermal spectral index² (α_{nt}) from sites of injection to regions of dominant energy loss. In Fig. 4 we also study the variation of $q_{20\text{cm}}$ (left) and $q_{90\text{cm}}$ (right) with the α_{nt} determined at scales of $\sim 1 - 1.5 \text{ kpc}$ for all these galaxies from Basu et al. (2012). The distribution of α_{nt} with steps of 0.05, are shown in the top panels (Figure 10 in Basu et al. 2012). The right panels shows the distribution of q_λ for the respective frequencies with steps of 0.05. The shaded histograms represents the arms and the unfilled histograms are for the interarms. At $\lambda 20 \text{ cm}$ there is no apparent variation in the value of $q_{20\text{cm}}$ with α_{nt} (Pearson’s correlation coefficient, $r = 0.27$), while at $\lambda 90 \text{ cm}$ the $q_{90\text{cm}}$ decreases with steepening of the α_{nt} ($r = 0.7$).

In the arm regions where α_{nt} is seen to have a narrow distribution with mean -0.8 and dispersion of 0.14 , the q_λ values are higher, suggesting $\tau_{\text{syn}} \gg \tau_{\text{esc}}$. However, in the interarm regions, α_{nt} and q_λ have a wide distribution with more than 50 percent dispersion. The values of ‘ q_λ ’ also systematically decreases as one moves from arms to interarms, indicating $\tau_{\text{esc}} \gg \tau_{\text{syn}}$ and thus the CRe loose energy before escaping the disk giving rise to steeper α_{nt} . Similar results were found for IC 342 and NGC 5194 (Murgia et al. 2005; Paladino et al. 2006).

4. DISCUSSION

We have studied the radio–FIR correlation at $\sim 1 \text{ kpc}$ scales for four normal galaxies using nonthermal radio maps at $\lambda 90 \text{ cm}$ and $\lambda 20 \text{ cm}$ and the far infrared maps at $\lambda 70 \mu\text{m}$. From the basic synchrotron theory (e.g., Moffet 1975) and considering the radio emission from

CRe emitting at critical frequencies, the energy of CRe at $\lambda 90 \text{ cm}$ is $\sim 1.5 \text{ GeV}$ and at $\lambda 20 \text{ cm}$ is $\sim 3 \text{ GeV}$ when they are gyrating in a typical magnetic field of $\sim 10 \mu\text{G}$. The far infrared emission at $\lambda 70 \mu\text{m}$ originates from cool dust at $\sim 20 \text{ K}$ heated by the interstellar radiation field (ISRF) due to $\sim 5 - 20 M_\odot$ stars (Devereux & Eales 1989; Xu 1990; Xu & Helou 1996; Dumas et al. 2011). We separately examine these correlations for the arm and the interarm regions, that is, regions of high and low thermal fractions respectively. The results of the various parameters as discussed in Section 3 are given in Table 3 for individual galaxies, and here we discuss the average properties. The dispersion on the parameter q_λ is a measure of the tightness of the radio–FIR correlation, which for the arm region is found to be less than 10 percent around the mean q_λ for both $\lambda 20 \text{ cm}$ and $\lambda 90 \text{ cm}$. For the interarm region the dispersion is seen to increase to around 20 percent for both the frequencies. Further we find the slope of the radio–FIR correlation for the arm regions (also the high thermal fraction regions) remains similar at both the radio frequencies (see Table 3). It should be noted that a large number of global scale radio–FIR correlation studies exist, where the observed slope is steeper and closer to unity (see e.g., Price & Duric 1992; Yun et al. 2001, and the references therein). However, the spatially resolved studies relating FIR cool dust emission to $\lambda 20 \text{ cm}$ radio emission, yields a value of the slope $\sim 0.6 - 0.9$ for LMC (Hughes et al. 2006) and 0.80 ± 0.09 for M31 (Hoernes et al. 1998). It is difficult to compare the slopes obtained in global studies with the spatially resolved case. The flux in global studies are averaged over both arm and interarm regions and we are uncertain about the contribution from each component. Multifrequency spatially resolved studies can provide an understanding of the relation between global scale and spatially resolved studies. For the present case, in the interarm regions (regions of low thermal fraction)

² In the text we define the spectral index α as, $S_\nu \propto \nu^\alpha$

for $\lambda 20$ cm the slope is slightly flatter as compared to the arms (see Eq. 1 and 2). However, at $\lambda 90$ cm, the slopes become distinctly flatter than the arm regions (see Fig. 2 and Eq. 3 and 4).

Our results can be used to determine the coupling between magnetic field (B) and the gas density (ρ_{gas}) as discussed in the introduction and thereby validating the ‘equipartition’ assumptions in these galaxies at 1 kpc scales. Dumas et al. (2011) showed that the slope of the radio–FIR correlation relates to κ as,

$$\kappa = \begin{cases} \frac{n b}{3 - \alpha_{\text{nt}}}, & \text{optically thick dust} \\ \frac{(n + 1) b}{3 - \alpha_{\text{nt}}}, & \text{optically thin dust} \end{cases} \quad (5)$$

where, $n = 1.4 \pm 0.15$ is the Kennicutt–Schmidt law index (see e.g., Kennicutt 1998), b is the slope of the radio–FIR correlation and α_{nt} is the nonthermal spectral index. For these face-on galaxies we use the assumption of optically thin dust to UV photons to estimate κ . We find that $\kappa = 0.51 \pm 0.1$ at $\lambda 20$ cm and $\kappa = 0.4 \pm 0.1$ at $\lambda 90$ cm. Similarly, for interarm regions due to a large range of α_{nt} we find κ in the range $0.41 - 0.5$ at $\lambda 20$ cm and between $0.18 - 0.22$ at $\lambda 90$ cm. Our estimated values of κ , using the correlation between $\lambda 20$ cm and $\lambda 70 \mu\text{m}$, are consistent with the predictions of numerical MHD simulations of different ISM turbulence models, where $\kappa \sim 0.4 - 0.6$ (see e.g., Fiedler & Mouschovias 1993; Kim, Balsara & Mac Low 2001; Thompson et al. 2006; Groves et al. 2003).

In the arm regions, the slope and thus κ remains similar for both $\lambda 20$ cm and $\lambda 90$ cm. Note that the above prescription to determine κ is valid provided the radio and the FIR emission arises from the same emitting volume, with a diameter of about 1 kpc for most of the observations reported here. In the arm regions the UV photon has a mean free path of ~ 100 pc within which most of the FIR emission arises. On the other hand, the CRe which gives rise to the radio emission diffuse farther away to ~ 1 kpc at 1400 MHz and ~ 2 kpc at 333 MHz in a galactic magnetic field of $\sim 10 \mu\text{G}$. Hence in order to have a similar slope with frequency, the energy spectrum of the CRe giving rise to the radio emission should be independent of the volume element. This can only happen if the timescale for CRe diffusion/propagation (τ_{diff}) is significantly larger than their generation timescale (τ_{gen}). It turns out that the τ_{diff} is about 8×10^7 yr at 333 MHz and 4×10^7 years at 1400 MHz which is significantly larger than the τ_{gen} as evident from the supernova rates, which is one every $10^4 - 10^5$ yr kpc^{-2} in Milky Way. We assume the same rate for these galaxies.

The slope of the radio–FIR correlation in the interarm (low thermal fraction) region is similar to that of the arm at $\lambda 20$ cm, however it becomes distinctly flatter at $\lambda 90$ cm. The flattening primarily happens due to relative increase in radio flux at $\lambda 90$ cm as compared to $\lambda 20$ cm, which has the effect that α_{nt} gradually becomes steeper in the interarms. This relative increase in $\lambda 90$ cm flux can be explained by continuous generation of CRe in the arm, which subsequently propagates into the interarm (e.g., from A to B or from farther regions in arms like C to B in Fig. 5). The propagation timescale for these CRe are

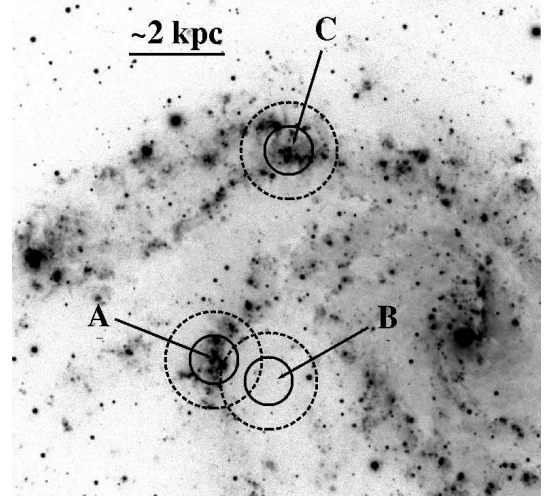


FIG. 5.— The $H\alpha$ image of the galaxy NGC 6946 (KPNO 2-m telescope, filter: KP1563) obtained from the ancillary data at SINGS website. The solid circles represents the diffusion scale of ~ 1 kpc for ~ 3 GeV CRe at $\lambda 20$ cm, while the dashed circles represents the diffusion scales of ~ 2 kpc for ~ 1.5 GeV CRe at $\lambda 90$ cm. See text for the details.

few times 10^7 years assuming Alfvén velocity of 100 km s^{-1} and typical arm to interarm distance of 1–2 kpc. In such a scenario, using Equation 6 of (Kardasev 1962), in a typical galactic magnetic field of $\sim 10 \mu\text{G}$, there would be a break in the energy spectrum for electrons above ~ 2 GeV. This break frequency lies below $\lambda 90$ cm or above 333 MHz. Such breaks have been seen at ~ 900 MHz and ~ 1 GHz for similar normal galaxies, NGC 3627 and NGC 7331 respectively (Paladino, Murgia & Orrù 2009). Thus the CRe emitting at $\lambda 90$ cm, which lie above the break, do not lose significant amount of energy as compared to their higher energy counterparts. Hence, this results in increasing the relative flux at $\lambda 90$ cm.

For the slope to remain similar between arms and interarm regions at $\lambda 20$ cm (below the break), the ratio of the radio to FIR flux densities should remain similar. Observed radio flux between arm and interarm changes by a factor of ~ 2 – 2.5 . Similar ratio of flux density between arm and interarm regions at $\lambda 20$ cm can be caused due to steepening of the spectral index to $\lesssim -1.1$ as compared ~ -0.6 to -0.8 in the arms. This implies the FIR flux should change by a factor of ~ 2.5 – 3 between arm and interarm regions for radio–FIR slope of ~ 0.8 . The FIR flux density (F_λ) depends on the dust temperature (T_{dust}) and its density (ρ_{dust}) as, $F_\lambda \propto \rho_{\text{dust}} Q_{\text{abs}}(a, \lambda) B_\lambda(T_{\text{dust}})$, where $Q_{\text{abs}}(a, \lambda)$ is the FIR wavelength (λ) dependent absorption coefficient for grain radius, a (Draine & Lee 1984; Alton et al. 2004). The temperature do not change significantly between arm and interarm for these galaxies (Basu et al. 2012). For a constant gas-to-dust ratio, i.e., $\rho_{\text{dust}} \propto \rho_{\text{gas}}$, a factor of 2–4 drop in average gas density between arm and interarm regions (found using the CO_{J:2→1} maps from Heracles; Leroy et al. 2009) would therefore cause the factor of 2–3 drop in FIR emission.

The slope of 0.8 ± 0.1 of the radio–FIR correlation indicates that the energy equipartition assumption between cosmic ray particles and magnetic field may be valid in the gas rich arms of the galaxies at our spatial resolution of ~ 1 kpc. For the interarm regions at $\lambda 20$ cm the slope

is similar to what is seen in arms, and thereby satisfying the equipartition conditions. The flattening of the slope at $\lambda 90$ cm does not indicate any break down of equipartition condition, but results due to overlapping emissions from adjacent regions.

We thank Adam Leroy for kindly providing us the FITS files for the CO_{J:2→1} moment-0 maps. We thank Yogesh Wadadekar for useful comments. We also thank

the anonymous referee for valuable comments. This research has made use of the NASA/IPAC Extragalactic Database (NED), which is operated by the Jet Propulsion Laboratory, California Institute of Technology, under contract with the National Aeronautics and Space Administration. This work is based (in part) on observations made with the *Spitzer Space Telescope*, which is operated by the Jet Propulsion Laboratory, California Institute of Technology under a contract with NASA.

REFERENCES

- Alton, P. B., Xilouris, E. M., Misiriotis, A., Dasyra, K.M., Dumke, M., 2004, A&A, 425, 109
- Appleton, P. N., et al., 2004, ApJS, 154, 147
- Basu, A., Mitra, D., Wadadekar, Y., Ishwara-Chandra, C. H., 2012, MNRAS, 419, 1136
- Beck, R., Golla, G., 1988, A&A, 191, L9
- Beck, R. 2007, A&A, 470, 539
- Berkhuijsen, E., 1997, in The Physics of Galactic Halos, eds. H. Lesch et al., (Berlin: Akademie-Verlag), 155
- Braun, R., Oosterloo, T. A., Morganti, R., Klein, U., Beck, R., 2007, A&A, 461, 455
- Chandrasekhar, S., Fermi, E., 1953, ApJ, 118, 113
- Cho, J., Vishniac, E. T., 2000, ApJ, 539, 273
- Cho, J., Lazarian, A., Vishniac, E., 2003, in Turbulence and Magnetic Fields in Astrophysics, ed. E. Falgarone & T. Passot (New York: Springer)
- Condon, J. J., 1992, ARAA, 30, 575
- Cox, M. J., Eales, S. A. E., Alexander, P., Fitt, A. J., 1988, MNRAS, 235, 1227
- Crutcher, R. M., 1999, ApJ, 520, 706
- Draine, B. T., Lee, H. M., 1984, ApJ, 285, 89
- Dressel, L. L., 1988, ApJ, 329, L69
- Devereux, N. A., Eales, S. A., 1989, ApJ, 340, 708
- Dumas, G., Schinnerer, E., Tabatabaei, F. S., Beck, R., Velusamy, T., Murphy, E., 2011, AJ, 141, 41
- Fiedler, R. A., Mouschovias, 1993, ApJ, 415, 680
- Groves, B. A., Cho, J., Dopita, M., Lazarian, A., 2003, PASA, 20, 252
- Harwit, M., Pacini, F., 1975, ApJ, 200, L127
- Helou, G., Soifer, B. T., Rowan-Robinson, M., 1985, ApJ, 298, L7
- Helou, G., Bica, M. D., 1993, ApJ, 415, 93
- Hoernes, P., Berkhuijsen, E. M., Xu, C., 1998, A&A, 334, 57
- Hughes, A., Wong, T., Ekers, R., Staveley-Smith, L., Filipovic, M., Maddison, S., Fukui, Y., Mizuno, N., 2006, MNRAS, 370, 363
- Isobe, T., Feigelson, E. D., Akritas, M. G., Babu, G. J., 1990, ApJ, 364, 104
- Kardasev, N. S., 1962, SvA, 6, 317
- Karachentsev, I. D., Sharina, M. E., Huchtmeier, W. K., 2000, A&A, 362, 544
- Karachentsev, I. D., Sharina, M. E., Dolphin, A. E., et al., 2002, A&A, 385, 21
- Karachentsev, I. D., Sharina, M. E., Dolphin, A. E., et al., 2003, A&A, 398, 467
- Kennicutt, Jr., R. C., 1998, ARAA, 36, 189
- Kennicutt, Jr., R. C., Armus, L., Bendo, G., et al. 2003, PASP, 115, 928
- Kim, J., Balsara, D., Mac Low, M.-M., 2001, JKAS, 34, 333
- Knapen, J. H., Stedman, S., Bramich, D.-M., Folkes, S. L., Bradley, T. R., 2004, A&A, 426, 1135
- Leroy, A. K., Walter, F., Bigiel, F., et al. 2009, AJ, 137, 4670
- Moffet, A. T., 1975, Stars and Stellar Systems Vol IX, Univ. Chicago Press, p211
- Murgia, M., Helfer, T. T., Ekers, R., Blitz, L., Moscadelli, L., Wong, T., Paladino, R., 2005, A&A, 437, 389
- Murphy, E. J. et al., 2006a, ApJ, 638, 157
- Niklas, S., Beck, R., 1997, A&A, 320, 54
- Paladino, R., Murgia, M., Helfer, T. T., et al., 2006, A&A, 456, 847
- Paladino, R., Murgia, M., Orrù, E., 2009, A&A, 503, 747
- Price, R., Duric, N., 1992, ApJ, 401, 81
- Rieke, G., et al., 2004, ApJS, 154, 25
- Tabatabaei, F. S., Beck, R., Krause, M., et al. 2007a, A&A, 466, 509
- Tabatabaei, F., Beck, R., Krugel, E., Krause, M., Berkhuijsen, E. M., Gordon, K. D., Menten, K. M. 2007b, A&A, 475, 133
- Thompson, T. A., Quataert, E., Waxman, E., Murray, N., Martin, C. L., 2006, ApJ, 645, 186
- de Vaucouleurs, G., et al. 1991, Third Reference Catalogue of Bright Galaxies (Berlin: Cambridge University Press)
- van der Kruit, P. C., 1971, A&A, 15, 110
- van der Kruit, P. C., 1973, A&A, 29, 263
- Wunderlich, E., Wielebinski, R., Klein, U., 1987, A&AS, 1987, 69, 487
- Xu, C., 1990, ApJ, 365, L47
- Xu, C., Klein, U., Meinert, D., Wielebinski, R., Haynes, R. F., 1992, A&A, 257, 47
- Xu, C., Helou, G., 1996, ApJ, 456, 163
- Yun, M. S., Reddy, N. A., Condon, J. J., 2001, ApJ, 554, 803